Global perturbation of stratospheric water and aerosol burden by Hunga eruption

Sergey Khaykin[1], Aurélien Podglajen[2], Felix Ploeger[3], Jens-Uwe Grooß[3], Florent Tence[1], Slimane Bekki[1], Konstantin Khlopenkov[4], Kristopher Bedka[4], Landon Rieger[5], Alexandre Baron[6], Sophie Godin-Beekmann[1], Bernard Legras[2], Pasquale Sellitto[7], Tetsu Sakai[8], John Barnes[9], Osamu Uchino[10], Isamu Morino[10], Tomohiro Nagai[10], Robin Wing[11], Gerd Baumgarten[11], Michael Gerding[11], Valentin Duflot[6], Guillaume Payen[12], Julien Jumelet[1], Richard Querel[13], Ben Liley[13], Adam Bourassa[5], Alain Hauchecorne[1], Francois Ravetta[1], Benjamin Clouser[14], and Artem Feofilov[15]

[1]Laboratoire Atmosphère Observations Spatiales, UVSQ, CNRS, Sorbonne University, France
[2]Laboratoire de Météorologie Dynamique, IPSL, CNRS, ENS-PSL/Sorbonne Univ., Paris, France
[3]Forschungszentrum Jülich, Institute of Energy and Climate Research (IEK-7), Jülich, Germany
[4]NASA Langley Research Center, Hampton, Virginia, USA
[5]Institute of Space and Atmospheric Studies, University of Saskatchewan, Saskatoon, Canada
[6]Laboratoire de l'Atmosphère et des Cyclones, UMR8105, University of La Réunion, CNRS, Météo France, La Réunion, France
[7]Univ. Paris Est Créteil and Université de Paris Cité, CNRS, Laboratoire Interuniversitaire des Systèmes Atmosphériques, Institut Pierre Simon Laplace, Créteil, France
[8]Meteorological Research Institute (MRI-JMA), Tsukuba, Japan
[9]NOAA Global Monitoring Laboratory, Boulder, Colorado, USA
[10]National Institute for Environmental Studies (NIES), Tsukuba, Japan
[11]Leibniz-Institut für Atmosphärenphysik, Kühlungsborn, Germany
[12]Observatoire des Sciences de l'Univers de la Réunion, UAR3365, University of La Réunion, La Réunion, France
[13]National Institute of Water & Atmospheric Research (NIWA), Lauder, New Zealand
[14]Department of the Geophysical Sciences, University of Chicago, Chicago, IL, USA
[15]LMD/IPSL, Sorbonne Université, UPMC Univ Paris 06, CNRS, École Polytechnique, Paris, France

November 22, 2022

Abstract

The eruption of the submarine Hunga volcano in January 2022 was associated with a powerful blast that injected volcanic material to altitudes up to 58 km. From a combination of various types of satellite and ground-based observations supported by

transport modeling, we show evidence for an unprecedented increase in the global stratospheric water mass by 13% as compared to climatological levels, and a 5-fold increase of stratospheric aerosol load, the highest in the last three decades. Owing to the extreme injection altitude, the volcanic plume has circumnavigated the Earth in only one week and dispersed nearly pole-to-pole in three months. The unique nature and magnitude of the global stratospheric perturbation by the Hunga eruption ranks it among the most remarkable climatic events in the modern observation era, with a range of potential persistent repercussions for stratospheric composition and climate.

Hosted file

`hunga_supplement_submission0.docx` available at https://authorea.com/users/535456/articles/599457-global-perturbation-of-stratospheric-water-and-aerosol-burden-by-hunga-eruption

Hosted file

`maps_refdif_p18_re3_21 hpa_wind_v2.gif` available at https://authorea.com/users/535456/articles/599457-global-perturbation-of-stratospheric-water-and-aerosol-burden-by-hunga-eruption

Hosted file

`sequencecthmapv2.gif` available at https://authorea.com/users/535456/articles/599457-global-perturbation-of-stratospheric-water-and-aerosol-burden-by-hunga-eruption

Global perturbation of stratospheric water and aerosol burden by Hunga eruption

Sergey Khaykin[1*], Aurelien Podglajen[2], Felix Ploeger[3], Jens-Uwe Grooß[3], Florent Tence[1], Slimane Bekki[1], Konstantin Khlopenkov[4], Kristopher Bedka[5], Landon Rieger[6], Alexandre Baron[7,8], Sophie Godin-Beekmann[1], Bernard Legras[2], Pasquale Sellitto[9,10], Tetsu Sakai[11], John Barnes[12], Osamu Uchino[13], Isamu Morino[13], Tomohiro Nagai[13], Robin Wing[14], Gerd Baumgarten[14], Michael Gerding[14], Valentin Duflot[7], Guillaume Payen[8], Julien Jumelet[1], Richard Querel[15], Ben Liley[15], Adam Bourassa[6], Alain Hauchecorne[1], François Ravetta[1], Benjamin Clouser[16], Artem Feofilov[17]

[1]Laboratoire Atmosphère Observations Spatiales, UVSQ, CNRS, Sorbonne University, France

[2]Laboratoire de Météorologie Dynamique, IPSL, CNRS, ENS-PSL/Sorbonne Univ., Paris, France

[3]Forschungszentrum Jülich, Institute of Energy and Climate Research (IEK-7), Jülich, Germany

[4]NASA Langley Research Center, Hampton, Virginia, USA

[5]Science Systems and Applications, Inc., Hampton, Virginia, USA

[6]Institute of Space and Atmospheric Studies, University of Saskatchewan, Saskatoon, Canada

[7]Laboratoire de l'Atmosphère et des Cyclones, UMR8105, University of La Réunion, CNRS, Météo France, La Réunion, France

[8]Observatoire des Sciences de l'Univers de la Réunion, UAR3365, University of La Réunion, La Réunion, France

[9]Univ. Paris Est Créteil and Université de Paris Cité, CNRS, Laboratoire Interuniversitaire des Systèmes Atmosphériques, Institut Pierre Simon Laplace, Créteil, France

[10]Istituto Nazionale di Geofisica e Vulcanologia, Osservatorio Etneo, Catania, Italy

[11]Meteorological Research Institute (MRI-JMA), Tsukuba, Japan

[12]NOAA Global Monitoring Laboratory, Boulder, Colorado, USA

[13]National Institute for Environmental Studies (NIES), Tsukuba, Japan

[14]Leibniz-Institut für Atmosphärenphysik, Kühlungsborn, Germany

[15] National Institute of Water & Atmospheric Research (NIWA), Lauder, New Zealand

[16]Department of the Geophysical Sciences, University of Chicago, Chicago, IL, USA

[17]LMD/IPSL, Sorbonne Université, UPMC Univ Paris 06, CNRS, École Polytechnique, Paris, France

Corresponding author: Sergey Khaykin (sergey.khaykin@latmos.ipsl.fr)

Abstract

The eruption of the submarine Hunga volcano in January 2022 was associated with a powerful blast that injected volcanic material to altitudes up to 58 km. From a combination of various types of satellite and ground-based observations supported by transport modeling, we show evidence for an unprecedented increase in the global stratospheric water mass by 13% as compared to climatological levels, and a 5-fold increase of stratospheric aerosol load, the highest in the last three decades. Owing to the extreme injection altitude, the volcanic plume has circumnavigated the Earth in only one week and dispersed nearly pole-to-pole in three months. The unique nature and magnitude of the global stratospheric perturbation by the Hunga eruption ranks it among the most remarkable climatic events in the modern observation era, with a range of potential persistent repercussions for stratospheric composition and climate.

Introduction

The main eruption of the Hunga submarine volcano (Tonga, 20.54°S, 175.38°W) on 15 January 2022 was likely the most explosive event of the modern observational era, with an estimated Volcanic Explosivity Index (VEI) of 5.8 (Poli and Shapiro, 2022). In the historical record, the Lamb wave triggered by the initial explosion is only comparable to that of the eruption of Mount Krakatoa in 1883 (Matoza et al., 2022; Wright et al., 2022). Stereoscopic analysis of geostationary satellite images shows that the volcanic plume reached up to about 58 km (Carr et al., 2022), resulting in the direct injection of volcanic gases and vaporised seawater from the magmatic chamber together with tropospheric moisture entrained by the eruptive updraft.

The dryness of the stratosphere is largely conditioned by the transit of the air masses through the cold tropical tropopause where freeze-drying usually limits the amount of water entering the stratosphere to a few ppmv (Brewer, 1949; Mote et al., 1996; Bonazzola and Haynes, 2004). As the atmospheric radiation budget is particularly sensitive to water vapour changes in the upper troposphere and lower stratosphere (e.g., Forster and Shine, 2002; Riese et al., 2012), even small changes in the stratospheric water content can lead to significant radiative forcing (Solomon et al., 2010) and alter stratospheric ozone chemistry (Anderson et al., 2012). The increase in stratospheric water vapour concentrations by a few ppmv simulated by current chemistry climate models in response to global warming may cause substantial positive climate feedbacks amplifying surface warming (Dessler et al., 2013). A rise in stratospheric water vapour also induces significant

changes in atmospheric circulation, increasing the poleward and upward shift of subtropical jet streams and intensifying the stratospheric Brewer-Dobson circulation by about 30% (Li and Newman, 2020), with further potential implications for surface climate.

Early studies of volcanic columns (e.g., Glaze et al., 1997) advocated that deep volcanic plumes, such as those of 1815 Tambora or 1883 Krakatoa, may have led to significant stratospheric hydration. Water vapor constitutes about 80% in volume of the erupted gas (Holland, 1978; Pinto et al., 1989) and a few percent of the total mass of ejected material which, for Hunga, ranges from 2,900 Tg (Yuen et al., 2022) to 13,000 Tg (Poli and Shapiro, 2022). Additional moisture may also be entrained from the troposphere (Glaze et al., 1997; Joshi and Jones, 2009). However, this stratospheric moistening conjecture had never been proven from observations. Due to condensation near the cold point tropopause, moderately explosive eruptions of the last two decades only generated limited water vapour injections, in contrast with their substantial impacts on the stratospheric sulfur and aerosol budget (Sioris et al., 2015; 2016). Pitari and Mancini (2002) proposed that the 1991 eruption of Mount Pinatubo injected about 37 Tg of water but this estimate was based solely on modeling considerations. The Hunga eruption on January 15, 2022 provides observational evidence for significant stratospheric hydration after a major volcanic eruption and recent studies (Millan et al., 2022; Xu et al., 2022) estimated that Hunga injected about 139 to 146 Tg of water into the stratosphere.

In this paper, we describe and quantify the stratospheric repercussions of the unique natural experiment in the middle atmosphere provided by the Hunga eruption. We investigate the formation and evolution of the stratospheric moisture and sulfate aerosol plume at a wide range of scales - from minutes and kilometres to monthly and planetary scales - using a synergy of satellite and ground-based observations supported by transport modeling. Given the outstanding magnitude of stratospheric moistening, and the absence of efficient sinks of moisture in the stratosphere, the Hunga eruption can be said to have initiated a new era in stratospheric gaseous chemistry and particle microphysics with a wide range of potential long-lasting repercussions for the global stratospheric composition and dynamics.

Volcanic injection into the middle atmosphere

While the Hunga eruptive sequence on January 15 (D+0) started around 04:05 UTC (Astafyeva et al., 2022), the paroxysmal blast occurred at 04:16 UTC (Poli and Shapiro, 2022; Matoza et al., 2022). At 04:25, the main volcanic plume reached its top recorded altitude of 58 km (Fig. 1A) with an ascent speed of at least 40 m/s over the previous 10 minutes, as shown by stereoscopic analysis of high-resolution imaging by GOES-17 and Himawari-8 geostationary satellites (Fig. S1A, Supplementary notes, Movie S1). The time evolution of the cloud top height reveals a complex eruption scenario of successive updrafts, in agreement with observations of infrasound waves suggesting three emission events (Podglajen et al., 2022). Numerical simulations of large eruptive columns (e.g. Woods, 1988) show that their temperature exceeds that of ambient air by hundreds of K at the tropopause. Thus, the initial plume has effectively bypassed the cold trap of the tropical tropopause and lower stratosphere.

The stratospheric umbrella cloud expanded at an altitude nearing 40 km within the first hour of the eruption to cover 150,000 to 200,000 km^2 (Fig. S1B).The dome of the ice cloud above 40 km, exposed to higher temperatures in the upper stratosphere (Fig. 1B), has entirely sublimated within an hour after the first blast (Fig. 1C). The lower umbrella, topping at around 35 km altitude, persisted longer and, carried by fast stratospheric easterlies, expanded 500 km to the West (Fig. 1A) and grew to 320,000 km^2 in three hours, nearly the size of Germany (Fig. S1B).
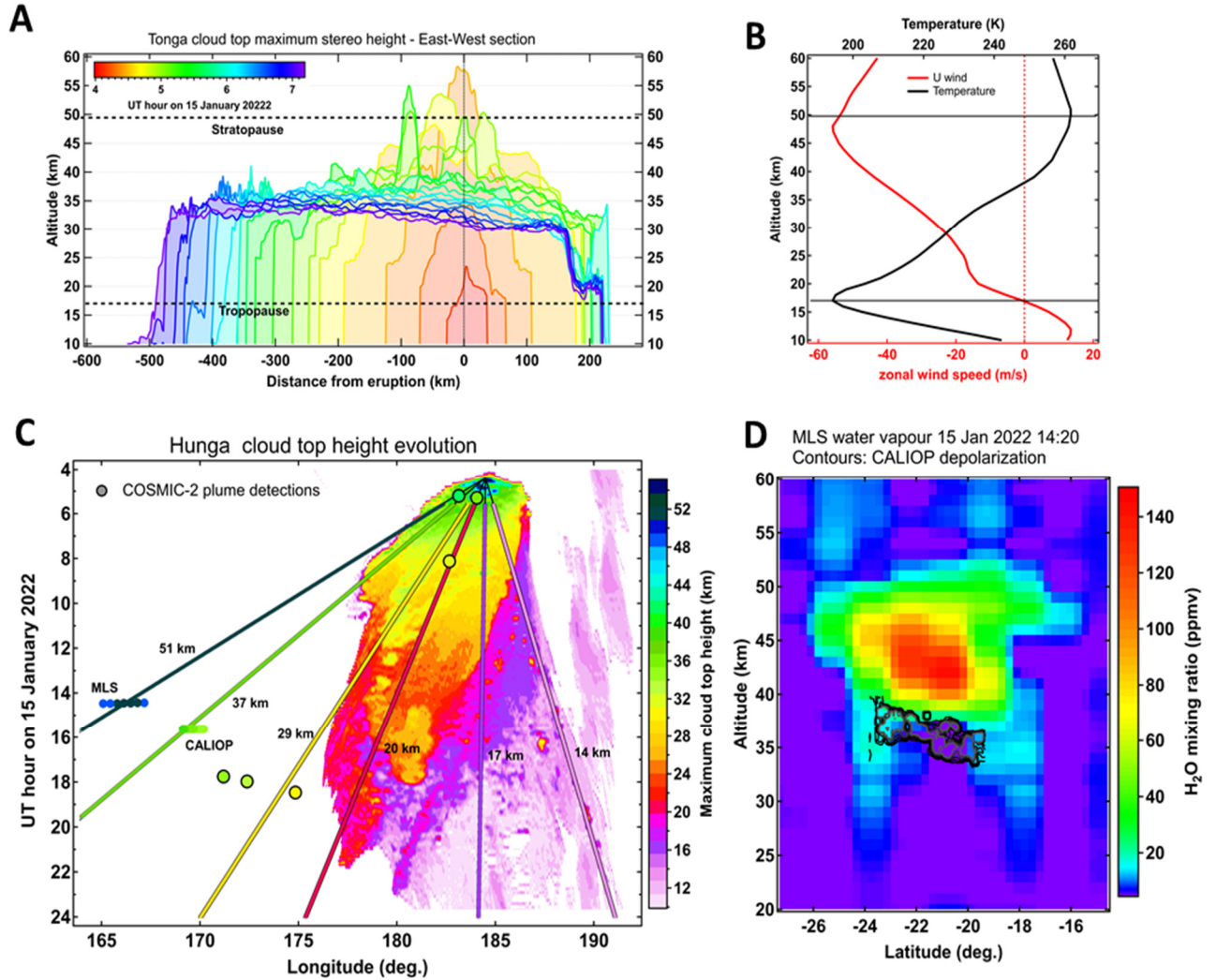
The formation and persistence of ice at such high altitude, although foreseen by modelling studies (Glaze et al., 1997; Textor et al., 2003), implies near ice-saturation and humidities more than three orders of magnitude larger than typically encountered in the stratosphere. Such near-saturation stratospheric water vapour in the plume is confirmed by Global Navigation Satellite System (GNSS) COSMIC-2 radio occultation soundings (hereafter GNSS-RO) on D0 downwind of the eruption (marked as circles in Fig. 1C). Extreme anomalies in bending angles and refractivity at altitudes of 30 to 40 km for about an hour after the eruption translate into strikingly-high stratospheric water vapour anomalies up to 15,000 ppmv at 37 km (Fig. S2B). Near saturation conditions are also revealed in later soundings and even persisted for 3 - 4 days at 20 - 30 km (Fig. S3).

In the case of a very fast injection such as that of Hunga, the main factors influencing the amount of water remaining in the stratosphere and hence the scavenging of volcanic gases by sedimenting ice appear to be the background temperature profile, plume top altitude and horizontal

123 extent of the umbrella cloud. Extrapolating the two early GNSS-RO profiles to the whole area of
124 the young umbrella cloud and neglecting the remaining ice leads to a stratospheric total water
125 injection lying between 100 - 150 Tg, similar to what would be obtained assuming a saturated
126 stratospheric column up to ~33 km. Comparison with later estimates of the mass of injected water
127 from Microwave Limb Sounder (MLS) observations showing 119 - 137 Tg (Fig. S6,
128 Supplementary notes) further suggests that the ice which survived fall-out and later sublimated
129 only plays a marginal role in the injection budget. The volume of water injected into the
130 stratosphere corresponds to the average amount of water discharged by the Amazon river
131 $(2.09 \times 10^5$ m^3/s) over about 10 minutes. Note that the peak volumetric discharge of the volcanic
132 plume was estimated at $\sim 9 \times 10^5$ m^3/s (Yuen et al., 2022).

133 The motion and lifetime of volcanic ice clouds at different heights (Fig. 1C) can be explained
134 by the easterly-sheared background flow and sublimation due to dilution within a warmer and drier
135 environment (Fig. 1B). At higher levels, the plume was subject to faster westward advection, but
136 also lower environmental humidity/higher temperatures towards the stratopause leading to a
137 quicker sublimation (within an hour at 40 km, after ~8 hours at 30 km). We note that vertical
138 motions, including sedimenting ice, also likely contribute to this evolution. Note that the ice plume
139 persisted the longest (about 20 hours) in the lower stratosphere, near the cold tropopause. Below
140 the tropopause (~17 km), the cloud drifted in the opposite direction (Fig. 1C) due to prevailing
141 upper-tropospheric westerlies (Fig. 1B).

142 The young outflow of the eruption was also sampled by MLS, revealing a ~12 km-thick layer
143 of strongly enhanced water vapour with a top at around 52 km (Fig. 1D) as well as by CALIOP
144 satellite lidar reporting a strongly depolarizing layer of particles between 35-40 km, just beneath
145 the moist plume (Fig. 1D). The high depolarization ratio of the plume suggests the presence of
146 non-spherical particles such as ash and/or ice.

Figure 1. Evolution of Hunga volcanic cloud top height (CTH) on the day of eruption (15 January 2022). (A) (A) East-West sections of maximum CTH color-coded by time from stereoscopic retrieval using Himawari-8 and GOES-17 geostationary imagers. (B) ECMWF temperature and zonal wind profiles averaged over 5º x 5º box centr`ed at the volcano location. (C) Hovmöller diagram of the maximum CTH (note the inverted time axis). Superimposed lines are color-coded by altitude and represent linear trajectories released from the location of volcano at different heights indicated in the panel. The circles colour-coded by altitude indicate the detections of water vapour and aerosol plumes respectively by MLS and CALIOP. The black-rimmed circles indicate the detections of hydrated layers by COSMIC-2 (Fig. S2B, Supplementary notes). Note the colour correspondence between the trajectories and downwind detections of the plume confirming the CTH retrieval. (D) Latitude-altitude cross section of water vapour from MLS (colour map) and depolarization ratio from CALIOP (contours, first contour is 0.05, interval is 0.05, last contour is 0.25). The time and longitude of MLS and CALIOP plume measurements are given in (C).
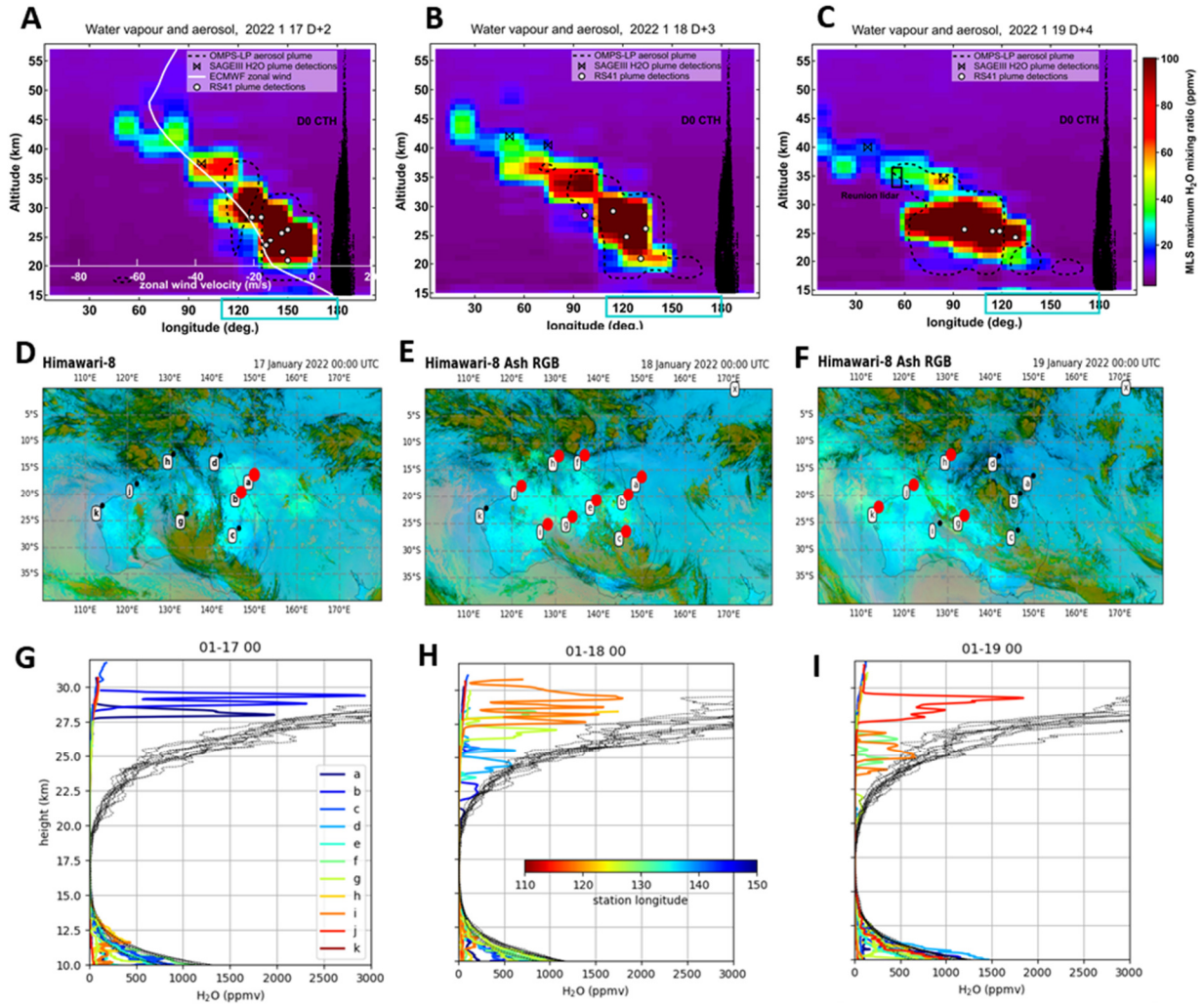
Early evolution of volcanic cloud

The explosive eruptive transport together with sedimentation and sublimation of ice produced a multitude of moist and aerosol-rich layers throughout the depth of the stratosphere. Their spatiotemporal evolution during the first days after eruption (D+2 to D+4), as observed by MLS (Fig. 2A, B, C), reveals a wind shear-shaped slant column of moisture extending throughout the stratospheric layer and spanning from Australia to Africa already on D+2. The strongly hydrated patches were accompanied by aerosol layers detected by OMPS-LP satellite instrument at all altitudes between the tropopause (~17 km) and 42.5 km. The presence of aerosols up to 37 km is confirmed by lidar measurements at La Reunion island downwind of Hunga on D+4 (Fig. 2C and S5B), which is the highest-level aerosol plume ever observed by ground-based lidars.

The primary volcanic cloud at lower altitudes (<~30 km), traceable by Himawari-8 volcanic RGB retrieval (Fig. 2D, E, F) was extensively sampled by the Australian upper-air meteorological network. The radiosondes showed numerous moist layers between 20 - 30 km with peak water vapour mixing ratios increasing with altitude from around 100 ppmv at 21 km to 2900 ppmv at 28 km following the physical limit of ice saturation at the given level (Fig. 2G, H, I).

The presence of large amounts of water in the volcanic plume has probably led to very fast oxidation of volcanic sulfur dioxide emissions to sulfuric acid (Zhu et al., 2022) - the main component of stratospheric aerosol droplets. According to CALIOP depolarization measurements, the aerosol particles were mostly spherical since D+1 and could therefore be characterized as sulfate aerosol droplets (Legras et al., 2022).

The primary aerosol plume at 27-30 km altitude, overpassing La Reunion island on D+6 - D+7, was marked by an unprecedentedly high optical depth of 0.8 and scattering ratio up to 280 at 532 nm (Baron et al., 2022) (Fig. S5B), which to our knowledge represents the most intense stratospheric aerosol plume ever observed by ground-based lidars.
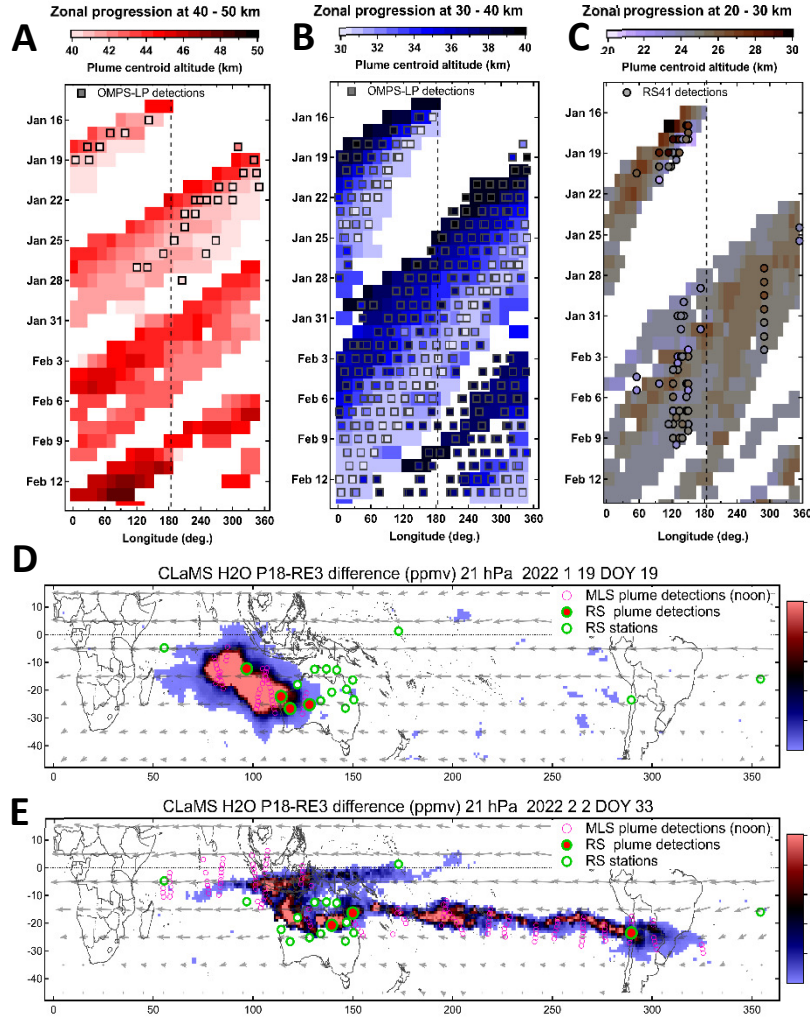
Figure 2. Early evolution of volcanic plume during 17-19 January 2022 (D+2 – D+4). (A, B, C) Longitude-altitude section of MLS maximum water vapour mixing ratio (WVMR) between 30S – 10S on the respective day. Black points indicate the ice cloud top height on the day of eruption (D0). The white curve represents the zonally-averaged ECMWF zonal wind profile. Black contours mark the areas where OMPS-LP detected aerosol layers with extinction ratio above 5. Diamonds and circles mark the detection of WVMR enhancements above 50 ppmv respectively by SAGE III and meteorological Vaisala RS41 radiosoundings. (D, E, F) Locations of the Australian radiosounding stations (marked a-k) superimposed on Himawary-8 Ash RGB images showing the extent of the primary volcanic plume as aquamarine area. The stations marked red represent the detections of WVMR enhancements. (G, H, I) Radiosonde profiles bearing WVMR enhancements above 50 ppmv on the respective day (marked by station and color-coded by longitude) and corresponding saturation mixing ratio profiles.

Fast circumglobal transport and vertical motion of moisture and aerosols

The extreme altitude reach of the Hunga eruption has led to an unusually fast circumglobal transport of volcanic material entrained by strong zonal winds in the upper stratosphere, up to 60 m/s at 47 km altitude (Fig. 2A). Consequently, the uppermost plume of moisture circumnavigated the Earth in only one week and made three full circles in 25 days whilst ascending through the Brewer-Dobson circulation from ~43 km to ~49 km (Fig. 3A), that is approximately 200 m per day. The aerosol plume above 40 km has travelled around the globe in 9 days and only made a single round. The limited lifetime of aerosols at this level could be due to sedimentation and/or evaporation of sulfate particles in the warm upper stratospheric environment (Kremser et al., 2016). We note though that the nature of the upper-stratospheric aerosols is unknown due to the absence of CALIOP depolarization measurements above 40 km.

In the middle layer (30 - 40 km), the aerosol and moisture plumes travelled in close tandem for about a month, circumnavigated the globe in 9 days and entirely covered the Southern tropical band by 29 January, that is in two weeks (Fig. 3B). Such a fast circumnavigation of the tropical stratosphere by a volcanic plume is remarkable compared to other major eruptions: the stratospheric plumes produced by 1982 El Chichon (Robock and Matson, 1983) and 1991 Pinatubo (Bluth et al., 1992) eruptions had circled the globe in three weeks, although their plumes were mostly confined to lower altitudes.

The zonal progression of the bulk of the plume contained within the 20-30 km layer is found to be fully consistent between MLS and radiosoundings, both showing a complete circumnavigation in two weeks (Fig. 3C). During its first circumnavigation, the plume undergoes significant subsidence, as seen from MLS and radiosounding data (Fig. 3C). We estimate an average descent rate around 200 m/day with maximum plume top altitudes decreasing from near 30 km during the first overpass over Australia (January 16-19) to ~26 km during the second overpass (February 1-10). Sellitto et al. (2022) proposed that this vertical motion be driven by radiative cooling induced by the large water vapor anomaly.
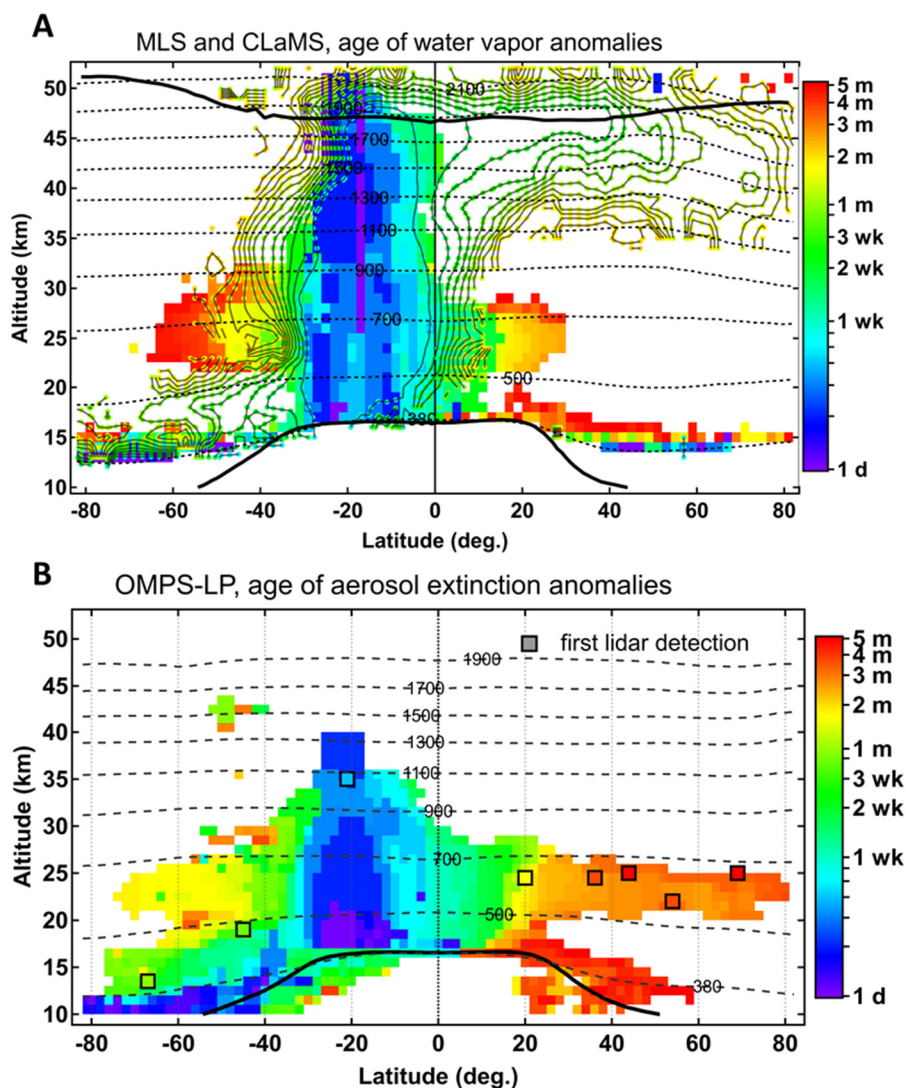
Figure 3. Circumglobal transport and morphological evolution of hydrated plumes. (A) Evolution of the water vapour mixing ratio (WVMR) peak altitude for the hydrated layers (WVMR>10 ppmv) in the upper stratosphere (40 – 50 km) as a function of time and longitude. The black squares with altitude-dependent colour meshing indicate the detections of aerosol layers with extinction ratio (ER>0.25)by OMPS-LP within the respective altitude range. Note that the uppermost plume at around 45 km circumnavigates the globe in only one week. (B) Same as A but for the hydrated layers (WVMR>10 ppmv) and aerosol layers (ER>2.5) in the middle stratosphere (30 – 40 km). (C) Same as (B) but for the lower tropical stratosphere (20 – 30 km) and with detection threshold of 30 ppmv. The black circles with altitude-dependent colour meshing indicate the radiosonde detections of WVMR enhancements above 50 ppmv. (D, E) Geographical extent of the hydrated plume during its first (D) to second (E) overpass above Australia from CLaMS model simulation. The values represent the WVMR difference between the control (pre-eruption initialization) and perturbed (post-eruption) simulations exceeding 3 ppmv at 21 hPa level (see Methods). The magenta open circles indicate the locations of MLS hydrated layers at 21 hPa with WVMR>30 ppmv. The green open circles show the locations of radiosounding stations involved in the analysis. The red-filled circles indicate the radiosonde detections of hydrated layers on the

246 respective day. ECMWF wind field at 21 hPa is shown in grey arrows. See Movie S2 for the
247 complete sequence.
248
249   Further insight into the morphological evolution of the volcanic moist plumes is provided by

250 simulations with the CLaMS chemistry-transport model (McKenna et al., 2002) initialised with

251 MLS water vapour observations (Supplementary notes). The simulation reveals a relatively

252 compact bulk plume during its first Australian overpass on D+4 (Fig. 3D), whereas during the

253 second overpass on 2nd February the plume appears as a dragon-shaped structure with a head

254 emerging around 10° S, where the Easterlies are strongest, and a tail at around 20° S extending

255 all across the Pacific (Fig. 3E and movie S2). The model simulated plume location, extent and

256 circumglobal transport is in good agreement with MLS satellite observations (Fig. 3 D-E, pink

257 circles; for further details see Supplementary notes). The cross-Pacific extent of the bulk plume by

258 the time of its first circumnavigation is also largely consistent with radiosonde detections of

259 hydrated layers (Fig. 3E).

260

261   **Meridional dispersion of volcanic plumes**

262   After being injected into the southern tropical stratosphere, the volcanic material is

263 subsequently transported in the meridional plane into Northern and Southern hemispheres by the

264 stratospheric circulation on a timescale of weeks to months (Fig. 4). The CLaMS simulation

265 vividly shows the transport towards the North pole along the deep branch of the Brewer-Dobson

266 circulation (BDC) on a timescale of 1-2 months as well as a fast isentropic transport towards the

267 South pole in the lowermost stratosphere (Fig. 4A). These pathways are consistent with the known

268 seasonality of the stratospheric BDC, with the deep branch circulation maximising in hemispheric

269 winter and the shallow branch circulation maximising in hemispheric summer (e.g., Konopka et

270 al., 2015). The MLS observations show that within five months of the eruption, the hydrated

271 plumes have spread in both directions from 65° S to 35° N but mostly within the bulk plume layer

272 (20 - 30 km). With that, the deep BDC transport pathway is not captured by MLS. These

273 differences between model and observations regarding meridional transport could be due to the

274 sensor sensitivity limits in the upper stratosphere and/or due to uncertainties in initial injection

275 height as represented in the model as well as due to uncertainty in the heating rates, which were

276 altered due to radiative cooling in the stratosphere induced by excessive moisture (Sellitto et al.,

277 2022).

278

Figure 4. Global dispersion of water vapour and aerosol plumes during five months since Hunga eruption. (A) Poleward dispersion of hydrated plumes detected by MLS with WVMR climatological anomalies exceeding 3 ppmv. The pixels are colour-coded by the age of hydrated layers since 15 January 2022. The contours (age colour-coding) represent the results of CLaMS model simulation of hydrated plumes transport (WVMR anomalies above 3 ppmv). Thick solid curves mark the tropopause and the stratopause, thin dashed curves indicate isentropic levels. (B) Same as A but for OMPS-LP detections of aerosol layers with extinction ratios exceeding 3. The black rectangles with age-dependent colour meshing indicate the first aerosol layer detections by ground-based lidars (see Fig. S5 and Supplementary notes).
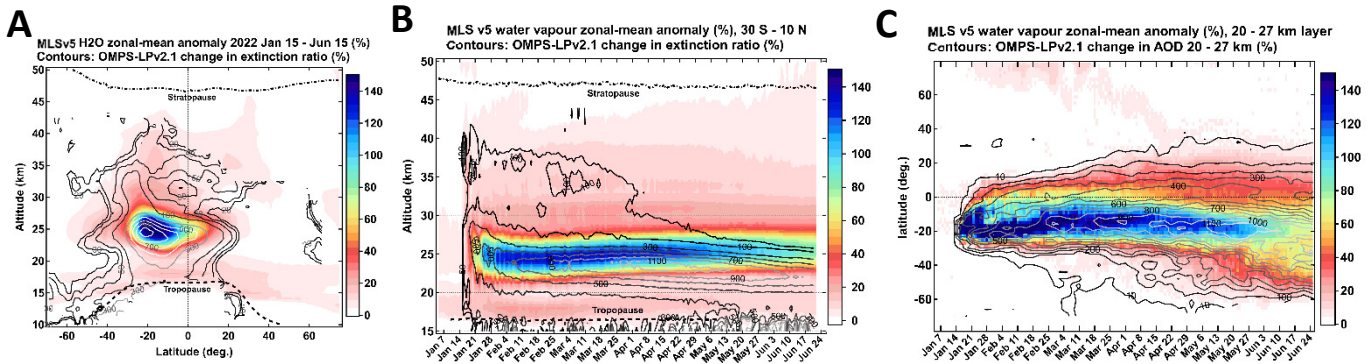
290   The meridional dispersion of aerosol plumes (Fig. 4B), as inferred from OMPS-LP
291 measurements, exhibits prominently the various transport pathways: the fast transport in the
292 lowermost stratosphere towards the South pole (3-4 weeks), the transport along the BDC between
293 500 K - 700 K isentropes into both hemispheres (1 - 2 months), which is followed by subsequent
294 dispersion from the Northern tropics towards the North pole (3 - 4 months). In the lower
295 stratosphere two distinct pathways emerge, likely involving confinement by the Asian and
296 American monsoon anticyclones resulting in the gap between the lower and upper branches. The
297 eventual occurrence of aerosols below the zonally-averaged tropopause level in the Northern and
298 Southern subtropics suggests sedimentation of large sulfate particles out of the stratosphere.

299   The satellite-derived meridional transport timescale is confirmed by ground-based lidar
300 detections of aerosol layers (Fig. S5, Supplementary notes) shown as black squares in Fig. 4B. The
301 fast transport towards the South pole within the lowermost stratosphere is captured by lidars at
302 Lauder station, New Zealand (45° S) and Dumont d'Urville French Antarctic station (67° S)
303 respectively 3 and 4 weeks after the eruption. The dispersion of sulfates to the Antarctic region
304 has thus occurred before the polar vortex formation, and the Dumont d'Urville lidar measurements
305 report stratospheric aerosol layers at the edge of the vortex in early June (not shown). The
306 northbound dispersion of aerosols is captured by lidar detections in the northern tropics (Mauna
307 Loa, Hawaii), subtropics (Tsukuba, Japan), mid-latitudes (OHP, France and Kuhlungsborn,
308 Germany) as well as high-latitudes (Alomar, Norway). Overall, in about three months since the
309 eruption, the Hunga sulfates have spread nearly pole-to-pole, although the aerosol layers detected
310 in the Northern extratropics are less intense, with scattering ratios below 1.8 (Fig. S5).

311

312 **Global perturbation of stratospheric water and aerosol burden**

313   The extreme explosiveness of the Hunga eruption has led to in-depth perturbations of
314 stratospheric gaseous and particulate composition. Figure 5A shows the broad-range positive post-
315 eruption water vapour anomaly (colours) that extends throughout the depth of the tropical
316 stratosphere - from the tropopause to nearly the stratopause. The region of highest anomalies,
317 exceeding 100% on a zonal-mean scale and averaged over 5 months after the eruption, is found in
318 the southern tropics within the 23 - 27 km altitude layer. The anomaly in aerosol extinction
319 (contours) exceeding 100% extends across most of the tropical lower and middle stratosphere and
320 reaches 1000% at 24-25 km altitude in the southern tropics. The latitudinal pattern of the aerosol

extinction anomaly is well correlated with that of water vapour, except for the downward shift of aerosol anomalies. Indeed, while the bulk layer of gaseous water and the upper boundary of the positive water anomaly are both gradually rising in the tropical upwelling branch of the Brewer-Dobson circulation, the bulk of aerosols is sedimenting with a vertical rate estimated as 0.26 mm/s (Fig. 5B, Fig. S7F). The subsidence and meridional dispersion of the bulk aerosol layer is well captured by Aeolus ALADIN satellite lidar (Fig. S10). Despite the vertical decoupling of bulk water vapour and aerosol layers in the stratosphere, their meridional dispersion reveals a very similar pattern with a more efficient transport towards the Southern pole (Fig. 5C).

Figure 5. Spatiotemporal structure of the stratospheric water vapour and aerosol burden perturbation. (A) MLS zonal-mean WVMR anomaly above 5% averaged over five months following the eruption with respect to MLS 17-yr climatology (%, color map) and OMPS-LP extinction ratio anomaly with respect to pre-eruption conditions (%, contours). (B) Same as A but as a function of time for the latitude band 30° S – 10° N. (C) Time-latitude variation of WVMR anomaly within 20-27 km altitude layer (color map) and change in OMPS-LP AOD with respect to the pre-eruption levels within the same layer (contours).
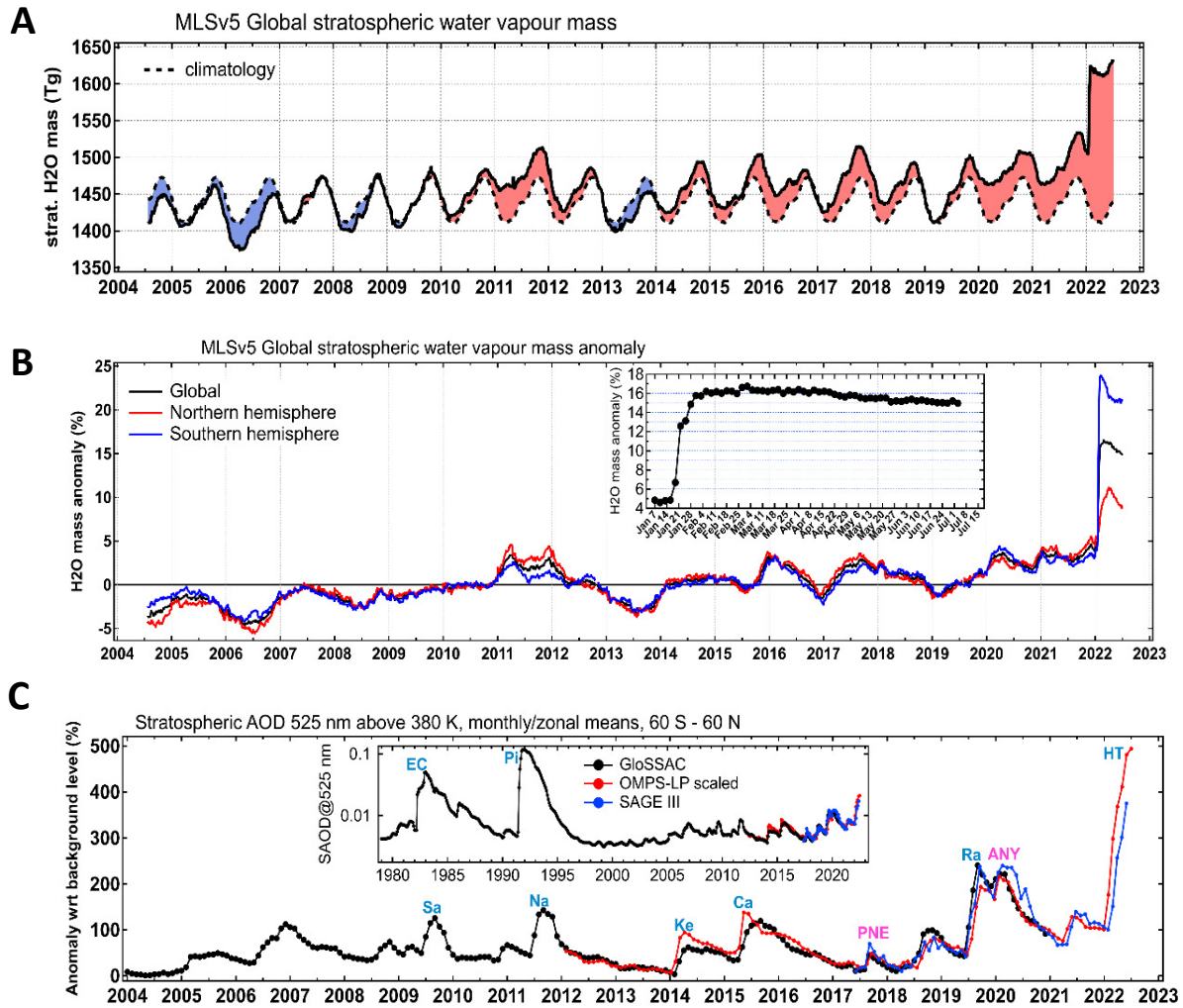
Figure 6A shows the annual cycle of stratospheric water vapour mass (between 100 hPa - 1 hPa pressure levels), which is characterised by a minimum in Boreal Spring and a maximum in Austral spring with a peak-to-peak amplitude of 60 Tg. The Hunga eruption occurred at the midpoint of the decay phase and boosted the stratospheric water burden by 119±6 Tg, which is nearly twice the annual amplitude. This figure is fully consistent with the GNSS radio occultation-based mass estimate of 100 - 150 Tg. Using an older V4 version of MLS data we obtain the mass of water transported across the 100 hPa level of 137±7 Tg, which is consistent with earlier estimates of 139 ±8 Tg by Xu et al. (2022) and 146±5 Tg by Millan et al. (2022). The stratospheric water burden perturbation by the Hunga eruption is about a factor of 5 larger than the previous

record-breaking perturbation of stratospheric water vapour (27 Mt) by the Australian "Black Summer" wildfires in 2019/2020 (Khaykin et al., 2020).

Figure 6B shows that the stratospheric water vapour mass anomaly has reached ~24% in the Southern and ~11% in the Northern hemisphere, whereas the global anomaly has reached ~16% after the eruption. Note that over the 17-yr time span of MLS data, the global and hemispheric anomalies do not exceed 5%, which renders the Hunga-induced perturbation of stratospheric water load unique in the record. Indeed, the Stratospheric Water and OzOne Satellite Homogenized data set (SWOOSH) (Davis et al., 2016) including satellite measurements of stratospheric water vapour since 1985, clearly shows that the perturbation is unprecedented in the satellite record of stratospheric water vapour.

The underwater blast associated with Hunga eruption and subsequent ice-vapour phase transition in the stratosphere led to a substantial increase in heavy water isotopologues as inferred from ACE-FTS data (Fig. S9, Supplementary notes). The extreme excursion of water isotopic ratio towards the Standard Mean Ocean Water (SMOW) levels strongly suggests seawater as the main source of injected moisture.
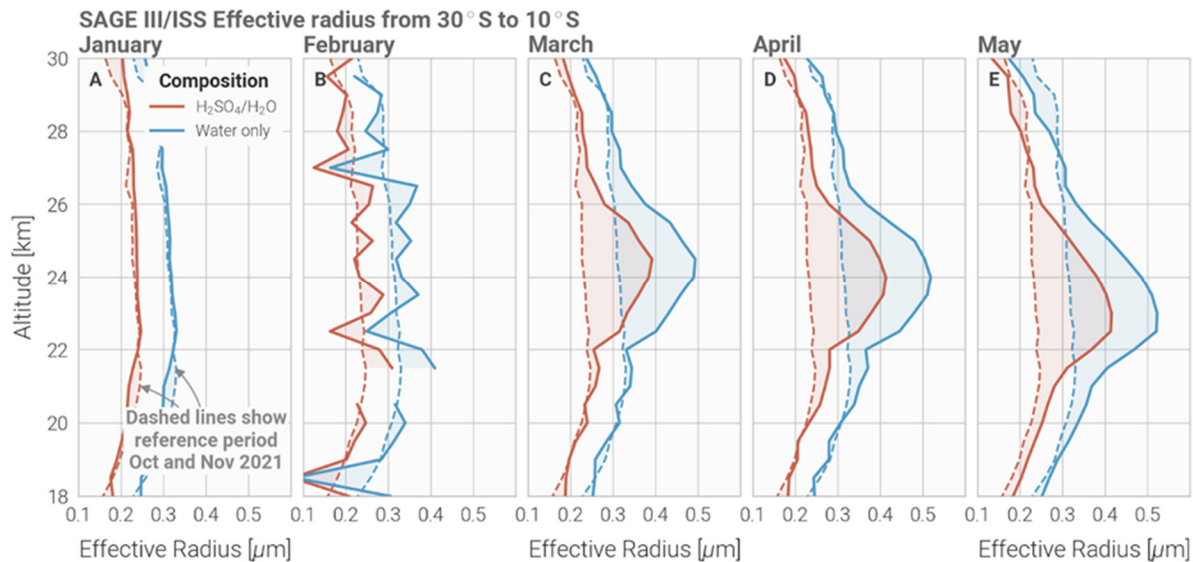
In order to place the stratospheric aerosol load perturbation by Hunga into historical perspective, we combined the GloSSAC merged satellite dataset (Kovilakam et al., 2020) spanning 1979-2020 with the recent aerosol extinction measurements by OMPS-LP and SAGE III satellite sensors. Figure 6C provides evidence that the Hunga eruption led to a 4-5-fold increase in the stratospheric aerosol optical depth (SAOD), exceeding by far any volcanic or wildfire event in the last three decades. With that, the absolute magnitude of SAOD perturbation (embedded panel in Fig. 6C) by Hunga is at least a factor of 6 smaller than to the previous major eruption of Pinatubo in 1991 and factor of 3 smaller than that of El Chichon in 1982.

Figure 6. Global perturbation of stratospheric water vapour and aerosol burden. (A) Evolution of the global MLS stratospheric water vapour mass (3-day averages) between 100 hPa – 1 hPa pressure levels (solid black curve) and climatological (2004-2021 period) annual cycle (dashed curve), the positive and negative anomalies are shown respectively as red and blue shading. (B) Deseasonalized stratospheric water vapour mass anomaly (per cent 3-day averages) for both hemispheres and the whole globe from MLS. The embedded panel shows the evolution of global anomaly in 2022. (C) Stratospheric aerosol optical depth (SAOD) anomalies for the 60⁰ S – 60⁰ N latitude band (monthly averages) from GloSSAC merged satellite record extended using OMPS-LP measurements at 675 nm scaled to 525 nm wavelength using GloSSAC data and SAGE III/ISS measurements at 521 nm converted to 525 nm using SAGEIII-derived Angstrom exponent. The SAOD anomalies are computed with respect to the background level estimated as GloSSAC SAOD average over volcanically-quiescent 1995-2003 period. The embedded panel shows the full time span of SAOD series. The cyan and pink letters indicate the most significant volcanic eruptions and wildfire events respectively (EC – El Chichon, Pi – Pinatubo, Sa – Sarychev, Na – Nabro, Ke – Kelud, Ca – Calbuco, PNE – Pacific Northwest wildfire event, Ra – Raikoke, ANY – Australian New Year wildfire event, HT – Hunga Tonga).

387   Of particular interest is the post-eruption evolution of stratospheric aerosol size. Figure 7
388   shows the effective radius retrieved from SAGE III for the months following the Hunga eruption
389   using different assumptions on the aerosol composition. Background conditions, shown in dashed
390   lines, typically have an effective radius of approximately 230 nm. After the eruption, particle size
391   increases from the background values to over 400-500 nm, depending on composition; larger than
392   at any other point in the SAGE III/ISS record. This growth is contained primarily between 22 and
393   26 km, which contains the bulk of the enhanced aerosol. By mid-March the particles have reached
394   their maximum size and this layer begins settling. A more detailed analysis of retrieved size
395   parameters suggests a complex interplay between the sedimentation, condensation and coagulation
396   processes (Supplementary notes, Fig. S8).

397   The sedimentation rate of aerosol was estimated from OMPS-LP tomographic retrieval of
398   extinction profiles by tracking the peak altitude of the plume (Supplementary notes and Fig. S7).
399   A linear fit to the peak beginning March 10th suggests a settling rate of 0.26 mm/s, which is in
400   agreement with CALIOP-derived estimates by Legras et al. (2022). Taking into account the
401   monthly averaged ERA5 vertical wind speed we obtain the fall speed, based on which the particle
402   size can be estimated using the method proposed by Kasten (1968). Depending on the assumption
403   on the particles' relative fraction of H_2O/H_2SO_4, we obtain a radius of 350 to 540 nm in April-
404   May, which is fully consistent with the SAGE III-derived particle sizes, providing confidence in
405   these estimates.

406

SAGE III/ISS Effective radius from 30°S to 10°S

Figure 7. Estimation of particle size from SAGE III/ISS multiwavelength data. Panels A-E show the monthly averaged retrieved effective radius from SAGE III/ISS assuming background (red) and pure-water (blue) aerosol composition. Dashed lines indicate the average effective radius pre-eruption, computed from October and November 2021 profiles.

Discussion

The extreme explosiveness of the Hunga eruption and the submarine location of the volcano add up to the unprecedented character, magnitude and the propagation timescale of the global stratospheric perturbation. The eruption provided a unique natural testbed, lending itself to studies of climate sensitivity to strong change in both stratospheric gaseous and particulate composition. In particular the effect on stratospheric water vapour is tremendous and expected repercussions range from persistent changes in atmospheric radiative balance (Santer et al., 2014; 2015) to amplification of the polar ozone depletion through wider occurrence of polar stratospheric clouds (Zhu et al., 2022).

The high persistence of the perturbation, related to the high injection altitude and extreme amount of stratospheric moisture together with the significant amount of sulfates generated by the Hunga eruption, will likely cause particularly long-lasting perturbations to atmospheric radiation and stratospheric chemistry. In six months since the eruption, the global anomaly of the stratospheric water burden did not decay more than 1-2%, and such persistence is expected

427   considering the absence of water vapour sinks in the middle stratosphere, that is where the bulk

428   layer of the Hunga moisture is contained.

429   While the longer-term aftermath of the Hunga effects is yet to be known, the available data

430   provide enough evidence to rank this eruption among the most remarkable climatic events in the

431   modern observational era and strongest in the last three decades. As remote sensing techniques

432   and satellite coverage of the stratosphere have been substantially improved in the XXI century, the

433   wealth of observational data on the Hunga event together with various modelling approaches

434   should provide a major advance in understanding the impacts of stratospheric composition change

435   on global climate.

448   **Author contributions:** SK conceived the study and performed analysis of MLS, OMPS-LP,
449   CALIOP, SAGEIII, GLoSSAC and CLaMS data; AP performed analysis of radiosoundings and
450   COSMIC-2 data, FP and JUG performed CLaMS simulation and analysis of MLS data, KK and
451   KB performed stereoscopic CTH retrieval; FT and SB computed stratospheric water vapour
452   masses; BLe provided Ash RGB data; LR computed particle radius from SAGEIII and OMPS-LP
453   data; TS, JB, OU, IM, TN, RW, GB, MG, AB, VD, GP, JJ, RQ, BLi, AH provided processed lidar
454   data; AF performed analysis of Aeolus data; BC performed analysis of ACE-FTS data; Ble, AP,
455   PS, SB, SGB, FR, AB were involved in discussions of the results and their interpretation. All
456   authors contributed to the final manuscript. The paper was written by SK, AP, FP, SB, LR, SGB,
457   JUG.

458   **Competing interests:** Authors declare that they have no competing interests.

459   **Data and code availability:** MLS water vapour data are available at
460   https://acdisc.gesdisc.eosdis.nasa.gov/data/Aura_MLS_Level2/ML2T.005/2022/. CALIOP data
461   v3.41 are available at: https://doi.org/10.5067/CALIOP/CALIPSO/CAL_LID_L1-
462   VALSTAGE1-V3-41. OMPS V2.0 data is available at https://snpp-
463   omps.gesdisc.eosdis.nasa.gov/data/SNPP_OMPS_Level2/OMPS_NPP_LP_L2_AER_DAILY.2/
464   2022/; OMPS-LP V2.1 data is available at
465   https://avdc.gsfc.nasa.gov/pub/data/satellite/Suomi_NPP/L2/LP-L2-AER-45km/LP-L2-AER-

474   **Methods**

475   *Stereoscopic cloud top height (CTH) retrieval*

476   Two primary steps were used in the derivation of cloud top height for the Hunga Tonga-
477   Hunga Ha'apai eruption cloud based on GOES-17 and Himawari-8 geostationary satellite
478   observations: 1) spatially matching simultaneous observations from the two satellites, and 2) using
479   the stereoscopy principle to construct a 3D profile of the cloud. Because the two satellites have
480   sufficiently different viewing angles, then it can be possible to derive a cloud top height with
481   accuracy equal to or better than the spatial resolution of the imagery being used. Level 1B infrared
482   (IR) brightness temperature (BT) data in the 10.3 μm is collected at 2 km/pixel nadir resolution
483   every 10 minutes and nearly simultaneously from GOES-17 and Himawari-8 because the imagers
484   on these satellites, the Advanced Baseline Imager (ABI) and Advanced Himawari Imager (AHI)
485   respectively, are nearly identical and have the same scan initiation times and scan rate. Although
486   IR imagery is of lower resolution than the visible, it has its own advantages as it is free of shadows,
487   is nearly isotropic, and is available at nighttime. Pixel geolocation in Level 1B data is obtained by
488   intersecting the instant view axis of the imager instrument with the Earth reference ellipsoid, and
489   thus the nominal image registration is accomplished assuming a zero elevation of observed scenes.
490   Once these Level 1B data are reprojected from the satellite's pixel/line space to a geographical
491   projection, any elevated scene exhibits a parallax displacement, which is different for images
492   recorded at different viewing angles. With simple geometric transformations, the two parallax
493   displacements from the two satellites can be directly related to the sought height.

494   An algorithm developed at NASA Langley Research Center uses image subsets (chips)
495   ranging from 8x8 to 20x20 pixel sizes to obtain a cross correlation between chips from the two
496   image sources. Trying different relative displacements between the chips consecutively yields the
497   highest correlation at the position of optimal displacement, which corresponds to the actual height
498   for that image subset. Analyses indicate that we were able to achieve a subpixel accuracy when

499 calculating the position of the highest correlation. This translates to a typical accuracy of the

500 derived height on the order of 0.2-0.4 km. When the analyzed image chips have little texture, the

501 correlation matching may fail for smaller chip sizes. In that case, a larger chip can be used to obtain

502 a reliable peak in the correlation profile, but that lowers the effective resolution of the resulting

503 map of retrieved heights. More than 90% of image chips, however, were reliably matched using

504 the 8x8 chip size, which helps to resolve smaller features and details within the eruption cloud,

505 like the small peaks of cloud extending above 50 km altitude. Overall, we estimate the spatial

506 resolution of the cloud top height retrieval product to be ~4-6 km/pixel. This algorithm was applied

507 to satellite data from 0400 to 2350 UTC on 15 January 2022 to quantify heights reached by the

508 eruption cloud and document its temporal evolution.

509 *COSMIC-2 water vapour retrieval*

510 Constellation Observing System for Meteorology Ionosphere and Climate (FORMOSAT-

511 7/COSMIC-2) (Schreiner et al., 2020) is a recently launched equatorial constellation of six

512 satellites carrying advanced GNSS (Global Navigation Satellite System) radio occultation (RO)

513 receivers, providing high vertical resolution profiles of bending angles and refractivity, which

514 contain information on temperature and water vapor. A few RO soundings occurred inside the

515 Hunga plume on January 15 th, depicting extremely unusual large refractivity anomalies. While

516 refractivity N in the neutral atmosphere depends on temperature T, pressure P, water vapor partial

517 pressure e and liquid water W (Kurskinky et al, 1997, equations 7 and 11):

518 $N = 77.6\, P/T + 3.73\ 10^5\, e/T^2 + 1.4\ W,$

519 the magnitude of the anomalies of the profiles in the early plume would result in temperature

520 anomalies with unphysically low values near the plume. On the contrary volcanic plume studies

521 suggest that the temperature within the plume relaxes to that of the background atmosphere within

522 a few tenths of minutes, with differences (e.g., associated with waves) below 10 K amplitude in

523 the stratosphere. Hence, we assume that the temperature is at environmental values, as given by

524 the high resolution operational analysis of the European Center for Medium Range Weather

525 Forecast (ECMWF), and attribute the refractivity anomaly signal solely to water vapor, in

526 agreement with expectations regarding the adjustment of a volcanic plume (Woods, 1988, Glaze

527 et al., 1997), which can be retrieved from (Kurskinky et al, 1997, equation 11):

528 $e = (N\ T^2 - b1\ P\ T)/(b2)$

MLS

The MLS (Microwave Limb Sounder) (Waters et al., 2006) instrument on the NASA Aura satellite has been measuring the thermal microwave emission from Earth's atmospheric limb since July 2004. With ~15 orbits per day, MLS provides day and night near-global (82° S–82° N) measurement of vertical profiles of various atmospheric gaseous compounds, geopotential height and temperature of the atmosphere. The measurements yield around to 3500 profiles per day for each species with a vertical resolution of ~3–5 km.

For this study we use version 5.01 MLS water vapour product. The data are accompanied by indicators about data quality and the status of the retrieval convergence. As stated by Millan et al. (2022), most of the early MLS measurements of the Hunga hydrated plume did not pass the MLS quality screening. Therefore, here we use MLS water vapour data without accounting for the quality flag as in Millan et al. (2022).

The stratospheric mass load of H_2O was derived from MLS volume mixing ratio measurements of water vapour in log pressure space, molecular mass of the compound and the air number density derived from MLS temperature profile on pressure levels between 100 hPa - 1 hPa levels. The error bars on the mass of injection are estimated by combining accuracies on the measurements and the mean standard deviations over 20-day periods before and after the sharp increase. See Supplementary notes for further detail on the mass estimation method.

CALIOP

The Cloud-Aerosol Lidar with Orthogonal Polarization (CALIOP) is a two-wavelength polarization lidar on board the CALIPSO mission that performs global profiling of aerosols and clouds in the troposphere and lower stratosphere (Winker et al., 2010). We use the total attenuated 532 nm backscatter level 1 product V3.40. The depolarization ratio is computed as the ratio between the perpendicular and parallel components of the attenuated backscatter.

OMPS-LP

The Ozone Mapping and Profiler Suite Limb Profiler (OMPS-LP) on the Suomi National Polar-orbiting Partnership (Suomi-NPP) satellite, which has been in operation since April 2012, measures vertical images of limb scattered sunlight in the 290-1000 nm spectral range (Jaross et al., 2014). The sensor employs three vertical slits separated horizontally to provide near-global

560   coverage in 3–4 days and more than 7000 profiles a day. Here we use OMPS-LP V2.0 aerosol

561   extinction data (Taha et al., 2021) at 675 nm for analysis of long-term stratospheric AOD evolution

562   (Fig. 6) and a special time period-limited V2.1 data version extended to 45 km altitude for the rest

563   of the analysis. Extinction ratio is computed as the ratio between aerosol and molecular extinction.

564   For estimating the sedimentation rate of aerosol particles, we use OMPS-LP data retrieved using

565   a tomographic algorithm (Zawada et al., 2018), which provides extinction profiles at 755 nm with

566   1- 2 km resolution throughout the stratosphere.

567

568   *Meteorological radiosoundings*

569   We use the data of meteorological radiosoundings conducted with high-accuracy Väisälä

570   RS41 sondes in the Southern tropics (Australia, Saint Helena island, Seychelles, Chile and

571   Argentina). Under normal circumstances, stratospheric humidity is particularly difficult to

572   measure due to low ambient relative humidity and large outgassing from the balloon (~100 ppmv

573   at 30 km) overwhelming the small stratospheric water signal (e.g. Vömel et al., 2007). However,

574   this contamination is outweighed by the ultra-moist plume HT plume which clearly stands out

575   from background variability and exceeds uncertainties of Vaisala RS41 during its first round-the-

576   globe tour. The humid plume (RH>20%) within the relatively warm upper stratosphere (T>220 K)

577   constitutes a favorable environment for RS41 humidity measurements (Survo et al., 2015). While

578   only RS41 data are included in this survey, other lower resolution sondes detected the plume during

579   its first overpass (Vaisala RS92) whereas others did not exhibit significant enhancements (M10,

580   iMET).

581   Later on during the plume dispersion, the raw water vapor signal is diluted and becomes

582   difficult to isolate from the effect of altitude-dependent outgassing. It is nevertheless possible to

583   track the plume as an anomaly from a typical contamination profile defined as the 90% quantile

584   profile over one month for each station. This simple approach is sufficient for the second overpass

585   over continental stations but fails over tropical islands where outgassing exhibits significant

586   variability related to low level moisture and cloudiness profile.

587

588   *Himawari-8 Ash RGB*

589   The early stage evolution of the plume is tracked with a composite RGB product that benefits

590   from the sensitivity of the Himawari-8 8.5 µm band to SO2 and sulphate aerosols. The product is

based on the EUMETSAT Ash RGB recipe and uses the brightness temperatures (BT in K) of the three channels: 8.5, 10.4 and 12.3 µm. The recipe for the three colour indexes ranging from 0 to 1 is R = (BT(12.3) - BT(10.4) + 4)/6, G = (BT(10.4) - BT(0.85) +4)/9, B = (BT(10.4) - 243)/60. This product qualitatively distinguishes thick ash plumes or ice clouds (brown), thin ice clouds (dark blue) and sulphur-containing plumes (neon-green). Mixed ash/sulphur-containing volcanic species would appear in reddish and yellow shades. We stress that this satellite product cannot distinguish between SO2 and sulphate aerosols, which have overlapping spectral signatures in this spectral range (Sellitto et al., 2017) and both appear as neon-green.

CLaMS chemistry-transport model simulation

The evolution of the Hunga Tonga water vapour plume through the stratosphere has been simulated with the Chemical Lagrangian Model of the Stratosphere, CLaMS (e.g., McKenna et al., 2002). CLaMS is a 3d Lagrangian chemistry transport model with transport and chemistry offline driven by wind and temperature data from meteorological (re)analysis or climate models. Lagrangian model transport is based on the computation of forward trajectories with an additional parameterization of small-scale turbulent mixing processes, depending on the shear in the large-scale flow. The calculation of stratospheric water vapour in CLaMS is based on a freeze-drying parameterization depending on local saturation mixing ratios along the air parcel trajectories and a mean sedimentation velocity for ice, and additional chemistry for representing methane oxidation (e.g. Poshyvailo et al., 2018). This model representation of relevant de- and re-hydration processes together with CLaMS' Lagrangian transport scheme has been shown advantageous for reliably simulating the stratospheric water vapour distribution (e.g. Ploeger et al., 2013) and its trend (Konopka et al., 2022). Also the transport of volcanic plumes has recently been simulated realistically with CLaMS (Kloss et al., 2021).

For this study we used the operational analysis from the European Centre of Medium-range Weather Forecasts (ECMWF) for driving model simulations. Model transport in the stratosphere is formulated using a diabatic coordinate in the vertical (potential temperature) and the required diabatic heating rates have been calculated via a Morcrette scheme assuming clear-sky conditions (e.g. Konopka et al., 2007). We carried out a control simulation for unperturbed conditions, with stratospheric water vapour initialised with mixing ratios observed by MLS just before the Tonga eruption on 13 January 2022, and a perturbed simulation with water vapour initialised just after

622 the eruption on 18 January 2022. For preparing 3D water vapour initialisation fields, MLS

623 measurements (data version 5) have been mapped onto the closest synoptic time (12 UTC) using

624 forward/backward trajectories, and have subsequently been binned to a regular 1x3 degree latitude-

625 longitude grid on the respective MLS pressure levels (see above). Data gaps in these regularly

626 gridded MLS water vapour distributions related to the coarse satellite sampling have been filled

627 by interpolation from values around, before using these distributions for initialising the CLaMS

628 irregularly spaced Lagrangian model grid on 13 and 18 January 2022 via interpolation.

629

630 *Ground-based lidars*

631 We use aerosol backscatter measurements at 532 nm provided by ground-based lidars at

632 various locations to characterize the time scale of the meridional dispersion of Hunga aerosol

633 plumes. The aerosol plumes are detected as local maxima in scattering ratio exceeding 1.2. The

634 lidar stations involved in this study (sorted by latitude) are Dumont d'Urville (67° S), Lauder (45°

635 S), Reunion (21° S), Mauna Loa (20° N), Tsukuba (36° N), Haute Provence (44° N), Kuhlungsborn

636 (54° N) and Alomar (69° N). The description of the measurement stations and lidar instruments is

637 provided in Supplementary notes.

638

639 *SAGE III*

640 The Stratospheric Aerosol and Gas Experiment (SAGE) III/ISS provides stratospheric aerosol

641 extinction coefficient profiles using solar occultation observations from the International Space

642 Station (ISS) (Cisewski et al., 2014). These measurements, available since February 2017, are

643 provided for nine wavelength bands from 385 to 1550 nm and have a vertical resolution of

644 approximately 0.7 km. The SAGE III/ISS instrument and the data products have characteristics

645 nearly identical to those from the SAGE III Meteor mission. We use version V5.2 of SAGE III

646 solar occultation species data. Particle size is retrieved from SAGE III/ISS by fitting the extinction

647 spectrum from 384 to 1540 nm using a unimodal lognormal particle size distribution. Typically,

648 particles in the stratosphere are composed primarily of sulfuric acid and water with a 75/25 mix of

649 H_2SO_4/H_2O. This assumption impacts the particle size retrieval through the index of refraction,

650 which for background conditions is typically between 1.40 to 1.44, depending on wavelength. If

651 particles are more hydrated this may reduce the index of refraction. To estimate the upper bound

652 of the error due to the assumed index of refraction the retrieval is also performed assuming droplets

653 of pure-water, which leads to retrieved effective radii consistently 100 nm larger than when
654 particles have a H_2SO_4/H_2O mix.

655 ***GloSSAC merged satellite aerosol climatology***

656 The Global Space-based Stratospheric Aerosol Climatology (GloSSAC) is a 38-year
657 climatology of stratospheric aerosol extinction coefficient measurements by various satellite
658 instruments such as SAGE, OSIRIS, CALIOP (Kovilakam et al., 2020). Data from other space
659 instruments and from ground-based, aircraft and balloon-borne instruments are used to fill in key
660 gaps in the data set. Here we use GloSSAC V2.1 data on aerosol extinction at 525 nm.

661 ***ALADIN/Aeolus***

662 The European Space Agency's Aeolus satellite carries a Doppler wind lidar called ALADIN
663 (Atmospheric Laser Doppler INstrument), which operates at 355 nm wavelength and which can
664 separate the molecular (Rayleigh) and particular (Mie) backscattered photons (high spectral
665 resolution lidar, HSRL). The lidar observes the atmosphere at 35° from nadir and perpendicular to
666 the satellite track, its orbit is inclined at 96.97º, and the instrument overpasses the equator at 6h
667 and 18h of local solar time (LST). We use its L2A Aerosol/Cloud optical product (baseline 12
668 and above) retrieved with the help of Standard Correct Algorithm (Flament et al., 2021) and
669 available at 87 km horizontal resolution.

670 ***ACE-FTS***
671 The ACE-FTS (Atmospheric Chemistry Experiment Fourier Transform Spectrometer)
672 (Boone et al., 2020) is the primary instrument aboard SCISAT. It has been observing about 30
673 solar occultations per day since 2004, recording spectra between 750 cm-1 to 4400 cm-1 at a
674 spectral resolution of 0.02 cm-1 and an altitude resolution of 1-2 km. Volumetric mixing ratio
675 profiles of more than 30 trace gases can be inferred from these spectra, including those of H_2O and
676 HDO. In this study we use the Version 4.1/4.2 Level 2 VMR retrievals of H_2O and HDO. Vapor-
677 phase deltaD is derived from these quantities at altitude levels between 12 and 40 km. DeltaD is a
678 measure of the HDO/H_2O ratio in a sample relative to ratio found in Standard Mean Ocean Water
679 (SMOW). Flags from both species are used to assess retrieval quality and determine at which
680 altitude ranges retrievals were actually performed.

681

References

Anderson, J. G., Wilmouth, D. M., Smith, J. B., and Sayres, D. S.: UV Dosage Levels in Summer: Increased Risk of Ozone Loss from Convectively Injected Water Vapor, Science, 337, 835–839, https://doi.org/10.1126/science.1222978, 2012

Astafyeva, E., Maletckii, B., Mikesell, T. D., Munaibari, E., Ravanelli, M., Coisson, P., et al. (2022). The 15 January 2022 Hunga Tonga eruption history as inferred from ionospheric observations. Geophysical Research Letters, 49, e2022GL098827. https://doi-org.insu.bib.cnrs.fr/10.1029/2022GL098827

Bluth, G.J.S., Doiron, S.D., Krueger, A.J., Walter, L.S., Schnetzler, C.C., 1992. Global tracking of the SO2 clouds from the June 1991 Mount Pinatubo eruptions. Geophysical Research Letters 19, 151–154. https://doi-org.insu.bib.cnrs.fr/10.1029/91GL02792

Boone, C.D., P.F. Bernath, D. Cok, S.C. Jones, J. Steffen, Version 4 retrievals for the atmospheric chemistry experiment Fourier transform spectrometer (ACE-FTS) and imagers. Journal of Quantitative Spectroscopy and Radiative Transfer 247, doi.org/10.1016/j.jqsrt.2020.106939, 2020.

Bonazzola, M., and P. H. Haynes (2004), A trajectory-based study of the tropical tropopause region, J. Geophys. Res., 109, D20112, doi:10.1029/ 2003JD004356.

Brewer, A. W.: Evidence for a world circulation provided by the measurements of helium and water vapour distribution in the stratosphere, Q. J. Roy. Meteor. Soc., 75, 351–363, https://doi.org/10.1002/qj.49707532603, 1949.

Carr, J. L., Horváth, Á., Wu, D. L., & Friberg, M. D. (2022). Stereo plume height and motion retrievals for the record-setting Hunga Tonga-Hunga Ha'apai eruption of 15 January 2022. Geophysical Research Letters, 49, e2022GL098131. https://doi-org.insu.bib.cnrs.fr/10.1029/2022GL098131

Cisewski et al. The stratospheric aerosol and gas experiment (SAGE III) on the International Space Station (ISS) Mission. Proc. SPIE 9241, Sensors, Systems, and Next-Generation Satellites XVIII, 924107 (2014).Dessler, A. E., Schoeberl, M. R., Wang, T., Davis, S. M., and Rosenlof, K. H.: Stratospheric water vapor feedback, P. Natl. Acad. Sci. USA, 110, 18087–18091, https://doi.org/10.1073/pnas.1310344110, 2013

Davis, S. M., Rosenlof, K. H., Hassler, B., Hurst, D. F., Read, W. G., Vömel, H., Selkirk, H., Fujiwara, M., and Damadeo, R.: The Stratospheric Water and Ozone Satellite Homogenized (SWOOSH) database: A long-term database for climate studies, Earth System Science Data, doi:10.5194/essd-8-461-2016, 2016

Flament, T., Trapon, D., Lacour, A., Dabas, A., Ehlers, F., and Huber, D.: Aeolus L2A aerosol optical properties product: standard correct algorithm and Mie correct algorithm, Atmos. Meas. Tech., 14, 7851–7871, https://doi.org/10.5194/amt-14-7851-2021, 2021

Forster, P. M. de F., and Shine, K. P., Assessing the climate impact of trends in stratospheric water vapor, Geophys. Res. Lett., 29(6), doi:10.1029/2001GL013909, 2002

Jaross, G., Bhartia, P. K., Chen, G., Kowitt, M., Haken, M., Chen, Z., Xu, P., Warner, J., and Kelly, T.: OMPS Limb Profiler instrument performance assessment, J. Geophys. Res.-Atmos., 119, 4399–4412, https://doi.org/10.1002/2013JD020482, 2014

Glaze, L. S., Baloga, S. M., and Wilson, L. (1997), Transport of atmospheric water vapor by volcanic eruption columns, J. Geophys. Res., 102(D5), 6099– 6108, doi:10.1029/96JD03125.

Holland, H. D., The Chemistry of the Atmosphere and Oceans, Wiley-Interscience, New York, 1978

Hegglin, M., Plummer, D., Shepherd, T. et al. Vertical structure of stratospheric water vapour trends derived from merged satellite data. Nature Geosci 7, 768–776 (2014). https://doi.org/10.1038/ngeo2236

Joshi, M. M. and Jones, G. S.: The climatic effects of the direct injection of water vapour into the stratosphere by large volcanic eruptions, Atmos. Chem. Phys., 9, 6109–6118, https://doi.org/10.5194/acp-9-6109-2009, 2009

Kasten, Fritz. "Falling speed of aerosol particles." Journal of Applied Meteorology (1962-1982) 7.5 (1968): 944-947.

Khaykin, S., Legras, B., Bucci, S. et al. The 2019/20 Australian wildfires generated a persistent smoke-charged vortex rising up to 35 km altitude. Commun Earth Environ 1, 22 (2020). https://doi.org/10.1038/s43247-020-00022-5

Kloss, C., Berthet, G., Sellitto, P., Ploeger, F., Taha, G., Tidiga, M., Eremenko, M., Bossolasco, A., Jégou, F., Renard, J.-B., and Legras, B.: Stratospheric aerosol layer perturbation caused by the 2019 Raikoke and Ulawun eruptions and their radiative forcing, Atmos. Chem. Phys., 21, 535–560, https://doi.org/10.5194/acp-21-535-2021, 2021

Konopka, P., F. Ploeger, M. Tao, T. Birner, and M. Riese (2015), Hemispheric asymmetries and seasonality of mean age of air in the lower stratosphere: Deep versus shallow branch of the Brewer-Dobson circulation, J. Geophys. Res. Atmos., 120, 2053– 2066, doi:10.1002/2014JD022429

Konopka, P., Günther, G., Müller, R., dos Santos, F. H. S., Schiller, C., Ravegnani, F., Ulanovsky, A., Schlager, H., Volk, C. M., Viciani, S., Pan, L. L., McKenna, D.-S., and Riese, M.: Contribution of mixing to upward transport across the tropical tropopause layer (TTL), Atmos. Chem. Phys., 7, 3285–3308, https://doi.org/10.5194/acp-7-3285-2007, 2007

Konopka, P., Tao, M., Ploeger, F., Hurst, D. F., Santee, M. L., Wright, J. S., & Riese, M. (2022). Stratospheric moistening after 2000. Geophysical Research Letters, 49, e2021GL097609. https://doi-org.insu.bib.cnrs.fr/10.1029/2021GL097609

Kovilakam, M., Thomason, L. W., Ernest, N., Rieger, L., Bourassa, A., and Millán, L.: The Global Space-based Stratospheric Aerosol Climatology (version 2.0): 1979–2018, Earth Syst. Sci. Data, 12, 2607–2634, https://doi.org/10.5194/essd-12-2607-2020, 2020.

Kremser, S., et al.: Stratospheric aerosol - Observations, processes, and impact on climate, Rev. Geophys., 54, doi:10.1002/2015RG000511, 2016.

758   Kursinski, E. R., Hajj, G. A., Schofield, J. T., Linfield, R. P., and Hardy, K. R. (1997),
759 Observing Earth's atmosphere with radio occultation measurements using the Global Positioning
760 System, J. Geophys. Res., 102(D19), 23429– 23465, doi:10.1029/97JD01569

761   Legras, B., Duchamp, C., Sellitto, P., Podglajen, A., Carboni, E., Siddans, R., Grooß, J.-U.,
762 Khaykin, S., and Ploeger, F.: The evolution and dynamics of the Hunga Tonga plume in the
763 stratosphere, EGUsphere [preprint], https://doi.org/10.5194/egusphere-2022-517, 2022

764   Li, F., Newman, P. Stratospheric water vapor feedback and its climate impacts in the coupled
765 atmosphere–ocean Goddard Earth Observing System Chemistry-Climate Model. Clim Dyn 55,
766 1585–1595 (2020). https://doi.org/10.1007/s00382-020-05348-6

767   Matoza, R.S., Fee, D., Assink, J.D., Iezzi, A.M., Green, D.N., Kim, K., Toney, L., Lecocq,
768 T., Krishnamoorthy, S., Lalande, J.-M., Nishida, K., Gee, K.L., Haney, M.M., Ortiz, H.D.,
769 Brissaud, Q., Martire, L., Rolland, L., Vergados, P., Nippress, A., Park, J., Shani-Kadmiel, S.,
770 Witsil, A., Arrowsmith, S., Caudron, C., Watada, S., Perttu, A.B., Taisne, B., Mialle, P., Le Pichon,
771 A., Vergoz, J., Hupe, P., Blom, P.S., Waxler, R., De Angelis, S., Snively, J.B., Ringler, A.T.,
772 Anthony, R.E., Jolly, A.D., Kilgour, G., Averbuch, G., Ripepe, M., Ichihara, M., Arciniega-
773 Ceballos, A., Astafyeva, E., Ceranna, L., Cevuard, S., Che, I.-Y., De Negri, R., Ebeling, C.W.,
774 Evers, L.G., FrancoMarin, L.E., Gabrielson, T.B., Hafner, K., Harrison, R.G., Komjathy, A.,
775 Lacanna, G., Lyons, J., Macpherson, K.A., Marchetti, E., McKee, K.F., Mellors, R.J., Mendo-
776 Pérez, G., Mikesell, T.D., Munaibari, E., Oyola-Merced, M., Park, I., Pilger, C., Ramos, C., Ruiz,
777 M.C., Sabatini, R., Schwaiger, H.F., Tailpied, D., Talmadge, C., Vidot, J., Webster, J., Wilson,
778 D.C., 2022. Atmospheric waves and global seismoacoustic observations of the January 2022
779 Hunga eruption, Tonga. Science. https:// doi.org/10.1126/science.abo7063, published online 12
780 May 2022.

781   McKenna, D. S., Konopka, P., Grooß, J.-U., Günther, G., Müller, R., Spang, R., Offerman,
782 D. and Orsolini, Y., A new Chemical Lagrangian Model of the Stratosphere (ClaMS), 1,
783 Formulation of advection and mixing, J. Geophys. Res., 107(D16), doi:10.1029/2000JD000114,
784 2002

785   Mote, P. W., Rosenlof, K. H., McIntyre, M. E., Carr, E. S., Gille, J. C., Holton, J. R.,
786 Kinnersley, J. S., Pumphrey, H. C., Russell, J. M., and Waters, J. W. (1996), An atmospheric tape
787 recorder: The imprint of tropical tropopause temperatures on stratospheric water vapor, J.
788 Geophys. Res., 101(D2), 3989– 4006, doi:10.1029/95JD03422

789   Pinto, J. P., Turco, R. P., and Toon, O. B. (1989), Self-limiting physical and chemical effects
790 in volcanic eruption clouds, J. Geophys. Res., 94(D8), 11165– 11174,
791 doi:10.1029/JD094iD08p11165

792   Pitari, G., and E. Mancini (2002), Short-term climatic impact of the 1991 volcanic eruption
793 of Mt. Pinatubo and effects on atmospheric tracers

794   Ploeger, F., Günther, G., Konopka, P., Fueglistaler, S., Müller, R., Hoppe, C., Kunz, A.,
795 Spang, R., Grooß, J.-U., and Riese, M. (2013), Horizontal water vapor transport in the lower
796 stratosphere from subtropics to high latitudes during boreal summer, J. Geophys. Res. Atmos.,
797 118, 8111– 8127, doi:10.1002/jgrd.50636

798   Podglajen, A., Le Pichon, A., Garcia, R. F., Gerier, S., Millet, C., Bedka, K. M., Khlopenkov, K. V., Khaykin, S. M., and Hertzog, A.: Balloon-borne observations of acoustic-gravity waves from the 2022 Hunga Tonga eruption in the stratosphere, Earth and Space Science Open Archive, p. 16, https://doi.org/10.1002/essoar.10511570.1, 2022

Poli, P., & Shapiro, N. M. (2022). Rapid characterization of large volcanic eruptions: Measuring the impulse of the Hunga Tonga Ha'apai explosion from teleseismic waves. Geophysical Research Letters, 49, e2022GL098123. https://doi-org.insu.bib.cnrs.fr/10.1029/2022GL098123

Poshyvailo, L., Müller, R., Konopka, P., Günther, G., Riese, M., Podglajen, A., and Ploeger, F.: Sensitivities of modelled water vapour in the lower stratosphere: temperature uncertainty, effects of horizontal transport and small-scale mixing, Atmos. Chem. Phys., 18, 8505–8527, https://doi.org/10.5194/acp-18-8505-2018, 2018

Riese, M., Ploeger, F., Rap, A., Vogel, B., Konopka, P., Dameris, M., and Forster, P. (2012), Impact of uncertainties in atmospheric mixing on simulated UTLS composition and related radiative effects, J. Geophys. Res., 117, D16305, doi:10.1029/2012JD017751

Robock, A., & Matson, M. (1983). Circumglobal Transport of the El Chichón Volcanic Dust Cloud. Science, 221(4606), 195–197. http://www.jstor.org/stable/1691596

Santer, B., Bonfils, C., Painter, J. et al. Volcanic contribution to decadal changes in tropospheric temperature. Nature Geosci 7, 185–189 (2014). https://doi.org/10.1038/ngeo2098

Santer, B. D., et al. (2015), Observed multivariable signals of late 20th and early 21st century volcanic activity, Geophys. Res. Lett., 42, 500–509, doi:10.1002/2014GL062366.

Schreiner, W., Rocken, C., Sokolovskiy, S., Syndergaard, S., & Hunt, D. (2007). Estimates of the precision of GPS radio occultations from the COSMIC/FORMOSAT-3 mission. Geophysical Research Letters, 34(4), L04808. https://doi.org/10.1029/2006gl027557

Sellitto, P. and Legras, B.: Sensitivity of thermal infrared nadir instruments to the chemical and microphysical properties of UTLS secondary sulfate aerosols, Atmospheric Measurement Techniques, 9, 115–132, https://doi.org/10.5194/amt-9-115-2016, 2016

Sellitto, P., Sèze, G., Legras. B. (2017), Secondary sulphate aerosols and cirrus clouds detection with SEVIRI during Nabro volcano eruption. International Journal of Remote Sensing, 38 (20), 5657-5672

Sellitto, P., Podglajen, A., Belhadji, R., Boichu, M., Carboni, E., Cuesta, J., Duchamp, C., Kloss, C., Siddans, R., Begue, N., Blarel, L., 305 Jegou, F., Khaykin, S., Renard, J.-B., and Legras, B.: The unexpected radiative impact of the Hunga Tonga eruption of January 15th, 2022, preprint, in review, https://doi.org/10.21203/rs.3.rs-1562573/v1, 2022

Sioris, C. E., Zou, J., McElroy, C. T., Boone, C. D., Sheese, P. E., and Bernath, P. F.: Water vapour variability in the high-latitude upper troposphere – Part 2: Impact of volcanic eruptions, Atmos. Chem. Phys., 16, 2207–2219, https://doi.org/10.5194/acp-16-2207-2016, 2016

Solomon, S., K. H. Rosenlof, R. W. Portman, J. S. Daniel, S. M. Davis, T. J. Sanford, and G.-K. Plattner (2010), Contributions of stratospheric water vapor to decadal changes in the rate of global warming, Science, 327, 1219–1223, doi:10.1126/science.1182488

838 Survo, P., Leblanc, T., Kivi, R., Jauhiainen, H., and Lehtinen, R.: Comparison of selected in-
839 situ and remote sensing technologies for atmospheric humidity measurement, in: Proceedings of
840 the 19th Conference on Integrated Observing and Assimilation Systems for the Atmosphere,
841 Ocean and Land Surface, Phoenix, AZ, 4–8 January 2015, 13B.2, 2015

842 Stratospheric Water and Ozone Satellite Homogenized (SWOOSH) database,
843 https://csl.noaa.gov/groups/csl8/swoosh/, Last access 13 July 2022

844 Taha, G., Loughman, R., Zhu, T., Thomason, L., Kar, J., Rieger, L., and Bourassa, A.: OMPS
845 LP Version 2.0 multi-wavelength aerosol extinction coefficient retrieval algorithm, Atmospheric
846 Measurement Techniques, 14, 1015–1036, https://doi.org/10.5194/amt-14-1015- 315 2021, 2021

847 Vömel, H., David, D. E., and Smith, K. (2007), Accuracy of tropospheric and stratospheric
848 water vapor measurements by the cryogenic frost point hygrometer: Instrumental details and
849 observations, J. Geophys. Res., 112, D08305, doi:10.1029/2006JD007224

850 Waters, J. W. et al. The earth observing system microwave limb sounder (EOS MLS) on the
851 Aura satellite. IEEE Trans. Geosci. Remote Sens. 44, 1106–1121 (2006)

852 Winker, D. M. et al. The CALIPSO mission: a global 3D view of aerosols and clouds. Bull.
853 Am. Meteorol. Soc. 91, 1211–1230 (2010).

854 Woods, A.W. The fluid dynamics and thermodynamics of eruption columns. Bull Volcanol
855 50, 169–193 (1988). https://doi.org/10.1007/BF01079681

856 Xu, J.; Li, D.; Bai, Z.; Tao, M.; Bian, J. Large Amounts of Water VaporWere Injected into
857 the
858 Stratosphere by the Hunga Tonga–Hunga Ha'apai Volcano Eruption. Atmosphere 2022, 13,
859 912. https://doi.org/10.3390/atmos13060912

860 Yuen, D.A., Scruggs M.A.,, Spera F. J.,, Zheng Y.,, Hu H., McNutt S.R., Thompson G.,
861 Mandli K., Keller B.R., Wei S.S., Peng A.,, Zhou A., Mulargia F., Tanioka Y.,Under the surface:
862 Pressure-induced planetary-scale waves, volcanic lightning, and gaseous clouds caused by the
863 submarine eruption of Hunga Tonga-Hunga Ha'apai volcano, Earthquake Research Advances,
864 2022, https://doi.org/10.1016/j.eqrea.2022.100134.

865 Zawada, Daniel J., et al. "Tomographic retrievals of ozone with the OMPS Limb Profiler:
866 algorithm description and preliminary results." Atmospheric Measurement Techniques 11.4
867 (2018): 2375-2393.

868 Zhu, Y., Bardeen, C., Tilmes, S., Mills, M., Harvey, V., Taha, G., Kinnison, D., Yu, P.,
869 Rosenlof, K., Wang, X., Avery, M., Kloss, C., Li, 330 C., Glanville, A., Millan, L., Deshler, T.,
870 Portmann, R., Krotkov, N., and Toon, O.: 2022 Hunga-Tonga eruption: stratospheric aerosol
871 evolution in a water-rich plume, preprint, in review, https://doi.org/10.21203/rs.3.rs-1647643/v1,
872 2022

873